High-Resolution Microwave Near-Field Surface Imaging Using Resonance Probes

High-Resolution Microwave Near-Field Surface Imaging Using Resonance Probes

Oleksandr Malyuskin, Vincent Fusco, *Fellow, IEEE*

***Abstract*—A novel microwave high-resolution near-field imaging technique is proposed and experimentally evaluated in reflectometry imaging scenarios involving planar metal-dielectric structures. Two types of resonance near field probes - a small helix antenna and a loaded subwavelength slot aperture are studied in this paper. These probes enable very tight spatial field localization with the full width at half maximum around one tenth of a wavelength, λ, at λ/100–λ/10 stand-off distance. Importantly, the proposed probes permit resonance electromagnetic coupling to dielectric or printed conductive patterns which leads to the possibility of very high raw image resolution with imaged feature-to-background contrast greater than 10dB amplitude and 50 degrees phase. Additionally, high-resolution characterization of target geometries based on the cross-correlation image processing technique is proposed and assessed using experimental data. It is shown that printed elements features with subwavelength size ~ λ/15 or smaller can be characterized with at least 10dB resolution contrast.**

***Index Terms*— Near field, microwave high-resolution imaging, microwave measurement, aperture, field enhancement, helical antenna.**

I. Introduction

MICROWAVE reflectometry is widely used in non-destructive testing, assessment and characterization of man-made and naturally occurring materials, e.g. dielectric and metal structures [1]- [3], biological samples [4],[5] critical parts of buildings and constructions [6], etc. The advantages of microwave reflectometry include the possibility of low-power, real-time and non-contact operation with high sensitivity and high resolution imaging of the target [7]. Microwave reflectometry is an accurate, repeatable, relatively inexpensive tool which can be adapted for both laboratory and industrial environments [7]-[9]. A broad range of microwave imaging and testing scenarios has been studied in the past, particularly dielectric characterization [1], [10] real-time water quality assessment [11], detection of defects such as cracks, voids and corrosion precursors [12], and biological applications like skin cancer screening [4],[13]. In this paper we study the possibility of near-field high-resolution microwave reflectometry imaging of passive samples using resonant aperture-based and apertureless probes.

This work was supported by the Leverhulme Trust, UK through the Grant RPG-2013-117. The authors are with The Institute of Electronics, Communications and Information Technology, Queen's University Belfast, Belfast, BT3 9DT, U.K.
(e-mail: o.malyuskin@qub.ac.uk; v.fusco@ecit.qub.ac.uk)

A probe or a near field antenna is an essential part of a reflectometry system responsible for electromagnetic (EM) interaction with the sample and reflected signal collection. The EM characteristics and geometry of the probe define the sensitivity of the measurement system, spatial resolution and imaging feature-to-background contrast necessary for accurate microwave characterization of the object under test. The imaging contrast is defined as a difference between the reflected signal amplitude and/or phase between the background and the imaged object.

Near field probes designed to date can be generally divided into three categories: aperture-based [3], [12]-[17] apertureless [5], [18]-[20] and printed or metal-dielectric near field antennas [21],[22].

The most commonly used aperture-based probes are open-ended waveguides [1], [3],[13], various apertures in conductive screens [14], [17], [23] and ridged horns [24]. Open-ended waveguide probes feature simple construction, and efficient EM aperture excitation which allows them to be used with low-power signals. At the same time the spatial resolution of the open-ended waveguide probes is limited by the waveguide cross-section whose size is around a half- wavelength. Therefore for higher spatial resolution, higher operating frequencies are required which leads to higher cost and complexity of equipment and, generally, higher measurement noise level. Also the imaging contrast achieved with open-ended waveguide probes is moderate and normally does not exceed 3dB of the reflected signal magnitude [3], [12], [13]. A possibility to enhance the spatial resolution and imaging contrast of the open-ended waveguide probes using dielectric inserts was studied in [1], [22],[25] however it was shown that even though the imaging contrast is increased the spatial resolution remains diffraction-limited (~λ/2).

Subwavelength apertures in conductive screens enable deep sub-diffraction spatial resolution of the features of the sample-under-test [14], [15], [20]. The application of small apertures is limited, however, by a very low transmitted microwave power, decreasing as the third power of the aperture size [26]. This restricts the probes imaging stand-off distance and reduces signal-to-noise ratio and achievable imaging contrast. To overcome these drawbacks it has been proposed to employ small apertures in combination with resonance antennas or resonance conductive inserts positioned in the close proximity to [27] or inside the aperture [28], [29].

Apertureless probes are represented by electric monopole and dipole-type antennas [30], [31]. The most common of which is a tip of open-ended coaxial [18], [20], [32]. Open-ended coaxial probes enable very high spatial resolution (better than λ/50) in a wide band of operation frequencies, however

there are major drawbacks including low signal-to-noise ratio, very small, ~1dB, imaging contrast [4], [20], [32] resulting from a weak EM coupling of the probe to the imaged sample. Also the open-ended coaxial probe can only operate at very small stand-off distances or when placed in immediate contact with the sample.

A resonance dipole antenna positioned in parallel with the scanned surface provides much higher levels of EM coupling with the material [31], thus imaging contrast can be improved. However the spatial resolution of a resonance dipole antenna is relatively poor, limited to a half-wavelength in the along-the-dipole direction and approximately equal to the doubled stand-off distance in the across-the-dipole direction [33]. Also, imaging of conductive surfaces at close distances (<λ/10) is challenging due to the out-of-phase dipole image [34] mitigating electric current along the antenna.

Recently there has been a significant amount of work aimed at the design of EM field collimating and near field probing devices based on metal-dielectric structures such as dielectric cones [35] and partially metallized dielectric prisms [20], near field antennas [21], resonantly loaded apertures [36] and metamaterial lenses [37], [38]. Dielectric conical probes enable relatively high spatial resolution, ~λ/5, [35] with moderate imaging contrast (>3dB). Dielectric probes with sharpened and metallized tips allow order of magnitude higher spatial resolution [20] albeit with reduced imaging contrast. The operation of metamaterial probes and EM field collimators [37] is mostly based on the anti-resonance or destructive Fresnel interference of the near field beams. This leads to substantial attenuation of the received signal or the appearance of blind scan areas [38] which could reduce the application range of the devices.

In this paper, we study two resonant microwave probe types that enable fine spatial resolution while retaining very high imaging contrast: (a) loaded subwavelength slot aperture [29], [36] and (b) helix antenna [39]. Resonantly loaded apertures (LA) allow significant enhancement of the electric and magnetic near fields as well as deep subwavelength field collimation in the near field zone [29], [36]. Due to this property very high imaging resolution is feasible along with a possibility of low power operation. The attributes of the classical helix antenna, operating in the normal radiation mode [39], which to the best of the authors' knowledge has not been studied before for near field imaging applications is also investigated. It is shown here that the near field of a helix antenna is tightly focussed in a beam with full width at half maximum (FWHM) ~ λ/10 at the ~ λ/20 stand-off distance which makes the helix antenna a promising near field probe. The commonality between these two probes is in their strong EM resonance along with the spatial near field confinement which makes them suitable for high-resolution near field imaging.

The imaging performance of these probes is evaluated using planar dielectric samples and printed circuit boards comprised of conductive elements printed on the FR4 dielectric substrate. These imaging scenarios are relevant in a wide range of applications including dielectric [36] and passive antenna arrays characterization. Special attention is given to the accurate characterization of the target geometry variation in printed arrays based on a simple cross-correlation technique.

Importantly the proposed probes can also be used for both electric and magnetic field imaging. The later due to the high intensity magnetic field focused in the near field zone [29], [36].

II. Imaging Setup

The one-port imaging setup geometry is shown in Fig.1 for the case of the loaded aperture, LA, probe. The LA probe is mounted on the NSI-200V-5x5 planar near-field scanner [40] with scan directions in the *xy* plane. The sample is held in a vertical position on a wooden frame (not shown in Fig.1) such that it is parallel to the scanning plane. The setup for the helix antenna is the same. As the probe scans the scene, varying near-field probe-sample EM coupling is transformed into the reflection parameter S_{11} amplitude and phase variation which forms a raw reflection image of the sample under test.

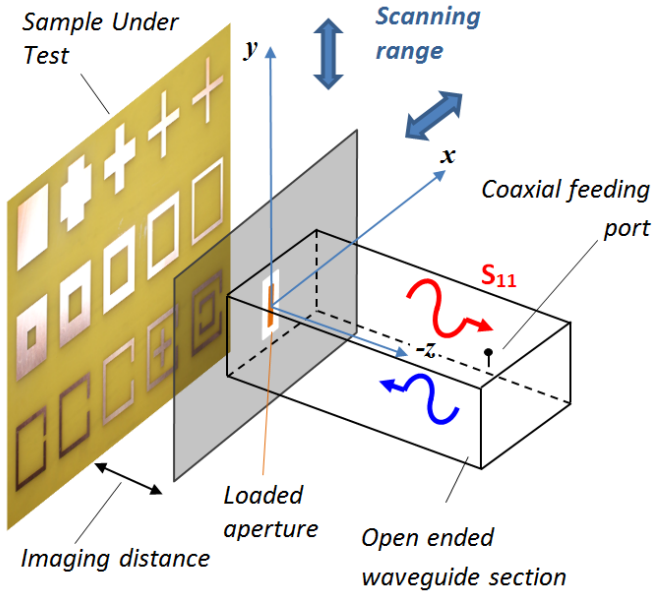

Fig.1.Imaging setup geometry for the case of LA probe.

The measurement were conducted at different power levels of the input source NSI SC 5911 from -30dBm to 10dBm with excellent stability of S_{11} parameter (amplitude deviation less than 0.3dB, phase deviation is less than 3 degrees). At input source power levels lower than -30dBm the stability of the measurements reduces (average S_{11} amplitude deviation ~1.5dB, phase deviation ~7-10 degrees). All measured results below in this paper are presented for 0dBm input source power. For the same source power level the measurements are repeatable with almost 100% accuracy.

In the next Section we discuss in details the geometry and EM properties of the LA and helix antenna probes.

III. Resonance Microwave Near-Field Probes

Two types of resonant near field probes are considered in this Section: a folded strip loaded subwavelength slot aperture [29] and a helix antenna [39].

A. Loaded Aperture Probe

The geometry of the dual screen LA probe is shown in Fig.2. The major advantage of this type of probe is its ability to collimate and significantly enhance the transmitted near field [29] due to a high-quality electric current resonance. The total length $L_1+2L_2+2L_3$ of the folded insert is ~ λ/2, slot length L_{sl} ~ λ/4 and slot width w_{sl} ~ λ/10. The insert is made of copper strip and supported by thin PVC film (~10μm) attached to front and back side of the dual screens. The separation between the screens h_s is ~ λ/20, strip width w_{str} ~ λ/50. The dimensions of the probe designed for 4GHz frequency are summarized in Table I. The aperture is excited by the TE_{10} mode (with E_y component of the EM field) propagating in the open-ended WR-187 waveguide section (frequency range 3.96GHz-5.85GHz) with flange dimensions 47.5x22.1mm, which is fed by a coaxial port, Fig.2. A very strong resonance of the electric currents flowing along the folded insert occurs as a result of the resonance length (λ/2) of the insert and the slot boundaries presence which act as a subwavelength resonator leading to considerable electric charge separation.

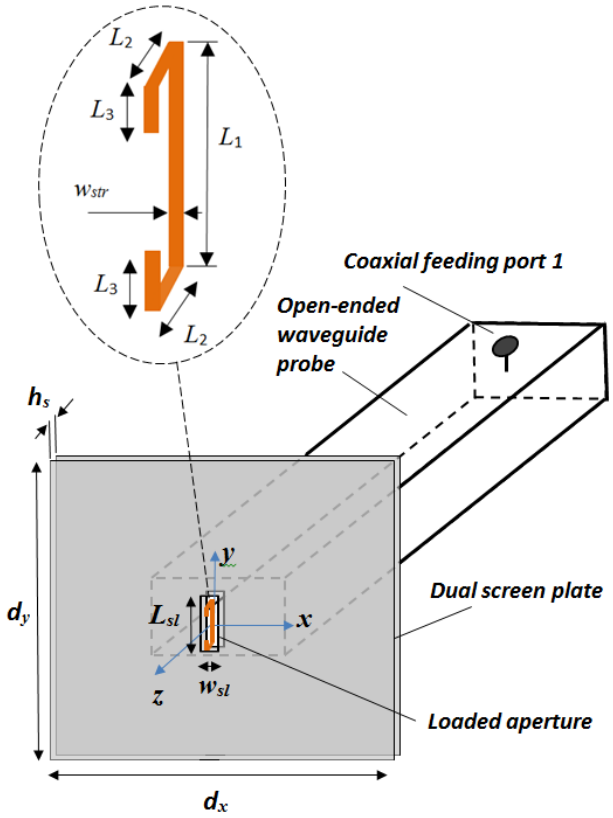

Fig.2.Geometry of the LA microwave probe.

The simulated (FEKO) near *E*-field amplitude distribution in the *xy* plane at z=4mm (λ/20) at frequency 4GHz is shown in Fig. 3. In the *E*-field dual hot spots, the electric field magnitude transmitted through the loaded aperture is around 25dB higher than the electric field magnitude of the unloaded aperture [29]. The *E*-field of the probe has two dominant components E_y and E_z around the near field focal zones.

TABLE I

DIMENSIONS (MM) OF THE LOADED APERTURE PROBE

d_x	d_y	h_s	L_{sl}	w_{sl}	L_1	L_2	L_3	w_{str}
66	66	3	25	7	18	3	6	2

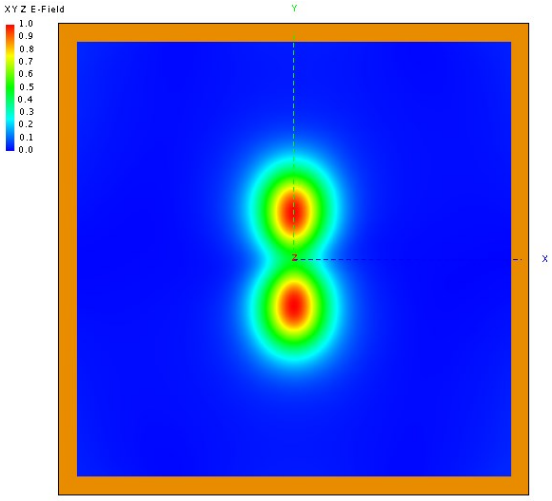

Fig.3. Normalized *E*-field amplitude at z=4mm stand-off distance in the xy plane.

B. Helix Antenna

The geometry of a helix antenna fed by a coaxial cable is shown in Fig.4.

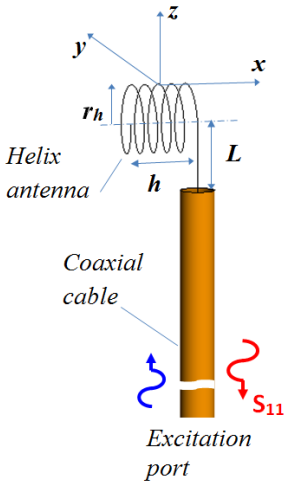

Fig.4.Geometry of the helix microwave probe. The parameters of the helix antenna designed for ~4GHz frequency are h=5.5mm, r_h= 2mm, L=8mm, number of turns = 5.5, the coaxial cable outer diameter is 3.58mm.

The antenna designed for ~4GHz operates in normal radiation mode [39]. The *E*-field is tightly collimated in the near field zone, Fig.5, with dominant *E*-field component along the helix axis (E_x) and vertical field component E_z.

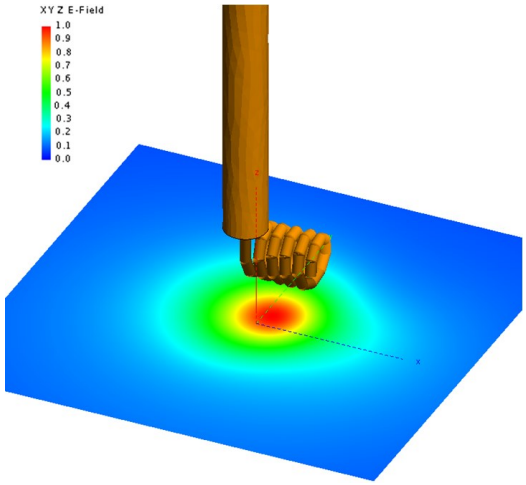

Fig.5. Normalized *E*-field amplitude at z=4mm standoff distance in the *xy* plane.

C. Comparison between the Helix Antenna and Loaded Aperture Probe

The measured reflection parameter S_{11} magnitude at the coaxial excitation port is shown in Fig.6 for the LA and helix antenna with parameters defined in Table I and in Fig.4. It can be seen that both probes support high-quality transmission resonance around 4.1GHz.

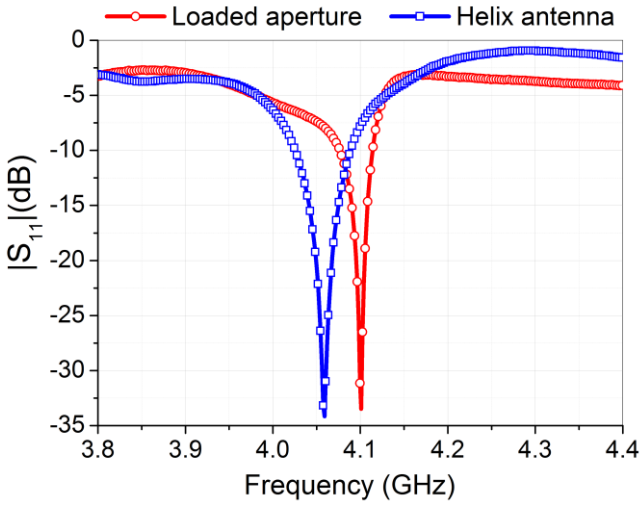

Fig.6. Measured S_{11} parameter magnitude in air for the LA and helix antenna probes.

Two major parameters that define microwave imaging resolution and sensitivity of the proposed probes are the near field spatial pattern FWHM and microwave power delivered to the focal spot (intensity of the field integrated across the spot area). The FWHM of the helix antenna and LA probe near field patterns are calculated at 4.1GHz using FEKO solver and summarized in Table II.

The loaded aperture probe produces a two-peak *E*-field distribution, Fig. 3(a), the FWHM is calculated for one of these peaks. It can be seen from Table II that the electric fields radiated by both probes are very well collimated (~λ/10) at 1mm-7mm range of stand-off imaging distances. The magnetic field of a helix antenna is collimated to ~ λ/10 spot in only in the vicinity of the probe at 1-2mm stand-off distance and then rapidly diverges. The magnetic field of the LA probe forms a beam, slowly divergent with the distance with FWHM ~ λ/15 and ~ λ/6 at 1mm and 7mm stand-off distance respectively.

TABLE II

FWHM OF PROPOSED MICROWAVE PROBES

Stand-off distance (mm)	Full Width at Half-Maximum (mm) at 4.1GHz			
	Helix Antenna		Loaded Aperture	
	$\|E\|$	$\|H\|$	$\|E\|$	$\|H\|$
1	3	5.8	3	5
2	5.5	8.2	6	9.7
3	6.8	15	7	9.52
4	8.5	27	8	9.88
5	10.4	35	9	10.4
7	15	>50	10.5	11.9

Fig. 7 shows the simulated dependence of the normalized *E*-field maximum in the hot spot in the air as a function of stand-off distance. From this graph it follows that the free-space *E*-field attenuation rate with stand-off distance is approximately the same for both probes, however the LA probe delivers around 15dB more of the microwave power to the focal spot than the helix antenna for the same input power from the source (0dBm). In Fig. 7, P_{LA} and P_{helix} is a total microwave power in the focal spot at -6dB level delivered by the LA and a helix antenna respectively. Efficient power delivery by a loaded aperture probe means that it could enable sensitive microwave imaging with high dynamic range.

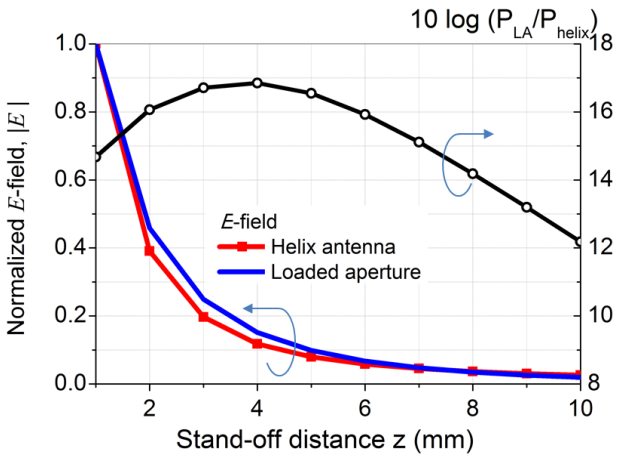

Fig.7.Simulated near zone *E*-field as a function of stand-off distance. Also the relative microwave power (field intensity integrated over the focal spot) for two types of resonant probes is shown by black line with hollow markers.

From the data presented in this Section it can be concluded that both the LA and helix antenna probes can operate as high-quality resonance near field probes with tightly collimated near field pattern, Table II, enabling high spatial resolution in a wide range of stand-off distances λ/100-λ/10. These probes have different EM coupling mechanisms in the presence of samples as will now be discussed.

IV. Imaging of Dielectric Samples

In this Section we study the resolution properties of the proposed resonance microwave probes for imaging of lossy dielectric planar structures. This imaging test is relevant in non-destructive characterization, dielectric quality control, etc. [1], [36].

A. Dielectric resolution chart

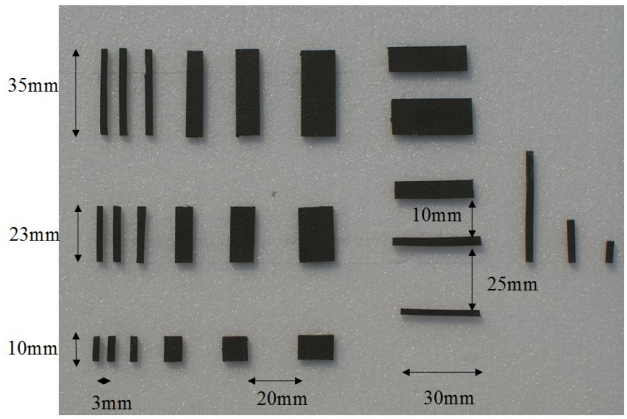

Fig.8. Lossy dielectric imaging test structure.

Fig. 8 shows the imaging test structure designed to reveal the characteristic resolution of the probes and achievable amplitude and phase imaging contrast. The structure is comprised of lossy dielectric strips of various lengths and widths attached onto a lossless 1cm thick Rohacell foam substrate (permittivity ~1.07). The lossy dielectric is 1mm thick Eccosorb FGM-U-40 layer with typical EM wave attenuation around 15dB/cm at 4GHz [41]. The characteristic dielectric constant of the FGM-U-40 is 10-2.0j at 4GHz. The scan steps Δx=Δy =2.0mm, scanning range 240mm in x direction and 200mm in y range, acquisition time around 7 minutes. The resonance center frequency is 4.06GHz and 4.05GHz in the case of the LA and helix probes respectively.

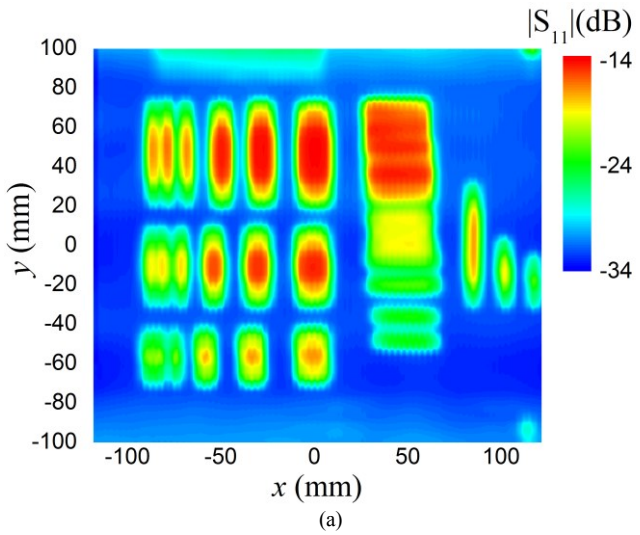

(a)

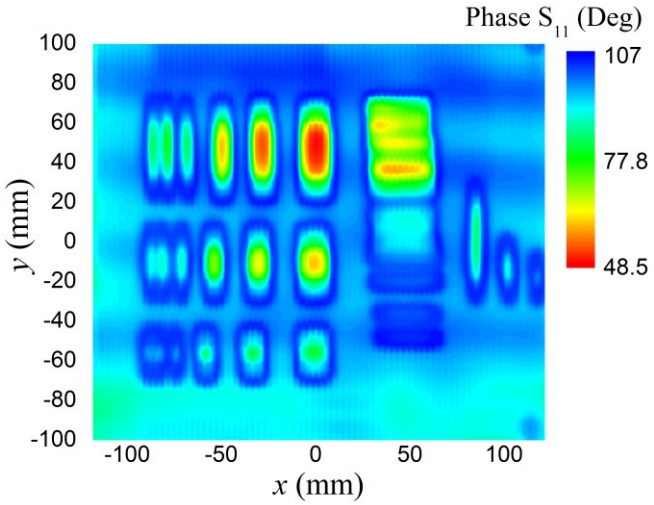

(b)

Fig.9. Amplitude (a) and phase (b) raw reflection image of the lossy dielectric imaging test at 4.06GHz obtained with LA probe. The imaging standoff distance is 4mm.

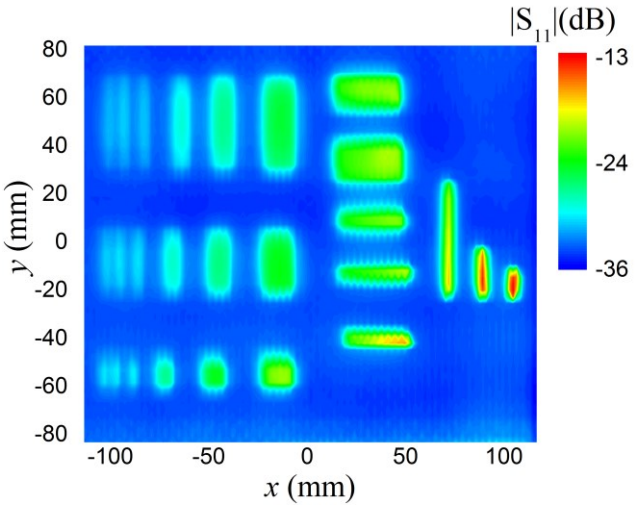

(a)

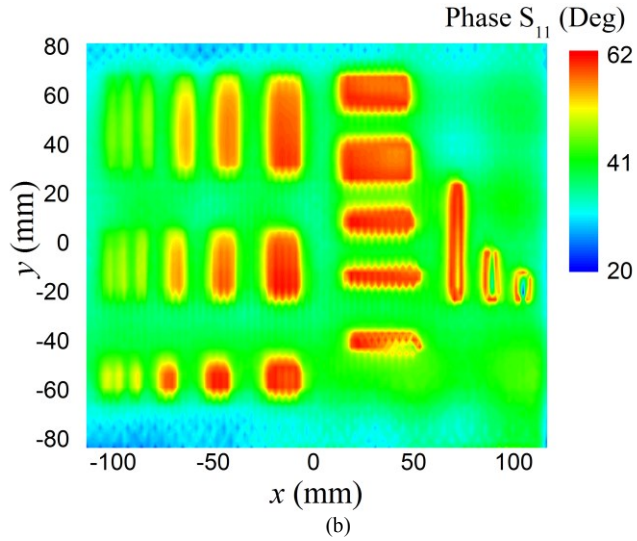

(b)

Fig.10. Amplitude (a) and phase (b) raw reflection image of the lossy dielectric imaging test at 4.05GHz obtained with a helix antenna probe. The imaging standoff distance is 4mm.

Raw amplitude (a) and phase (b) reflection images obtained with the LA probe and helix antenna are shown in Figs. 9 and 10 respectively for the standoff distance 4mm (median of the considered range of imaging distances). The LA aperture insert and the helix axis are aligned along the *y* direction.

It can be seen that the amplitude images display very high imaging contrast, more than 10dB amplitude for both the LA and helix probe, for the middle and top rows of strips starting separated in the *x* range by 5mm or more. The bottom row of strips displays much lower amplitude contrast 0.6-5dB due to strip length reduction. Phase images obtained with the LA probe, Fig. 9(b) possess much higher contrast, ~50 degrees, than the images obtained with the helix antenna, ~10 degrees, Fig. 10(b). It is worthwhile to note that even very small dielectric features ~λ/20 size can be clearly resolved in the sparse arrangements, both in amplitude and phase (e.g. three strips located at $x \approx 100$mm). Fig. 9 shows that the spatial resolution of the LA probe is limited in vertical direction by the insert length L_1~20mm, see e.g. an image of a column of horizontal strips located at 35mm< x <65mm.

B. Imaging distance

The data in Table II suggest that at smaller imaging distances the achievable spatial resolution could be better than 3mm (λ/25). It should be noted however that at very small imaging distances the resolution will be limited by two factors: (*i*) spatial size of the antenna, (*ii*) material EM loss. In the first case if the antenna near field footprint is such that the antenna couples to two features, they in general cannot be resolved. Therefore in the case of a helix probe, the resolution is approximately limited by the helix height *h* in the direction along the axis and limited by the helix diameter in the direction orthogonal to the helix axis. In the case of the LA probe the resolution is limited by the insert width w_{str} and length L_1 the *x* and *y* directions correspondingly. When the LA or helix probe is positioned in close proximity to a lossy dielectric sample, dielectric polarization leads to charge density

$$\rho(\vec{r}) = -\nabla \cdot (\varepsilon - 1)\vec{E}(\vec{r}) \qquad (1)$$

induced in the dielectric of permittivity ε due to the near field $\vec{E}(\vec{r})$ of the probe. Simulations (not presented here for brevity) show that the polarization charges lead to additional self-capacitance of the near field probe which causes resonance frequency shift, Fig.11.

Also material loss can result in substantial reduction of the near field antenna resonance quality, e.g. red line with circle markers in Fig. 11(a), (b), thus limiting the resolution contrast at very small stand-off distances. This effect is non-linear with the imaging distance z due to ~z^{-3} and ~z^{-2} spatial variation of the near field. At large standoff distances z ≥ 7mm (0.1λ) the near field beam of both probes diverges, Table II, the measured spatial resolution reduces to ~λ/8 in case of the LA probe and ~ λ/4 for a helical antenna.

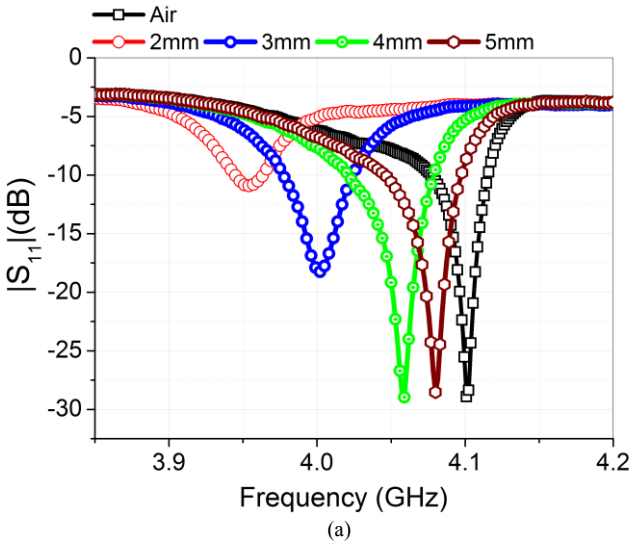

(a)

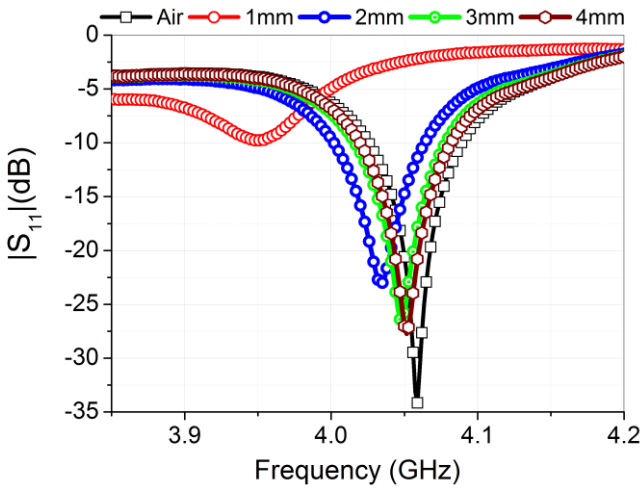

(b)

Fig.11. Resonance properties of the LA probe (a) and helix antenna (b) for a range of stand-off distances. The probes are positioned in the proximity of the 10x10cm FGM dielectric sheet of 1mm thickness.

C. Discrimination between lossy dielectrics

In this subsection a possibility of discrimination between lossy dielectric samples positioned on a lossy dielectric substrate is studied. The problem of dielectric discrimination arises in non-destructive testing and biomedical applications, e.g. skin cancer detection [4].

The imaged sample geometry is shown in Fig.12. Two left columns of dielectric strips are comprised of the BSR-U absorber material with microwave attenuation 21dB/cm at 4GHz, two right columns of strips are composed of GDS-U absorber material with 15dB/cm attenuation at 4GHz [41]. The strips are attached onto the 100mmx100mm sheet of FGM-U lossy dielectric material. The thickness of all sheets is 1mm.

Fig.13 shows the amplitude reflection images of the sample obtained with LA probe (a) and helix antenna (b) at 5mm and 2mm imaging distance correspondingly. Different stand-off imaging distance are chosen in order to achieve approximately the same imaging contrast.

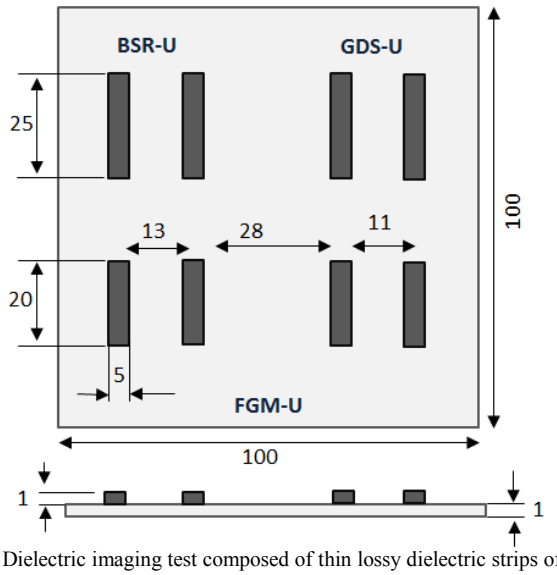

Fig.12. Dielectric imaging test composed of thin lossy dielectric strips of BSR and GDS material attached on a lossy dielectric substrate FGM. All dimensions in mm.

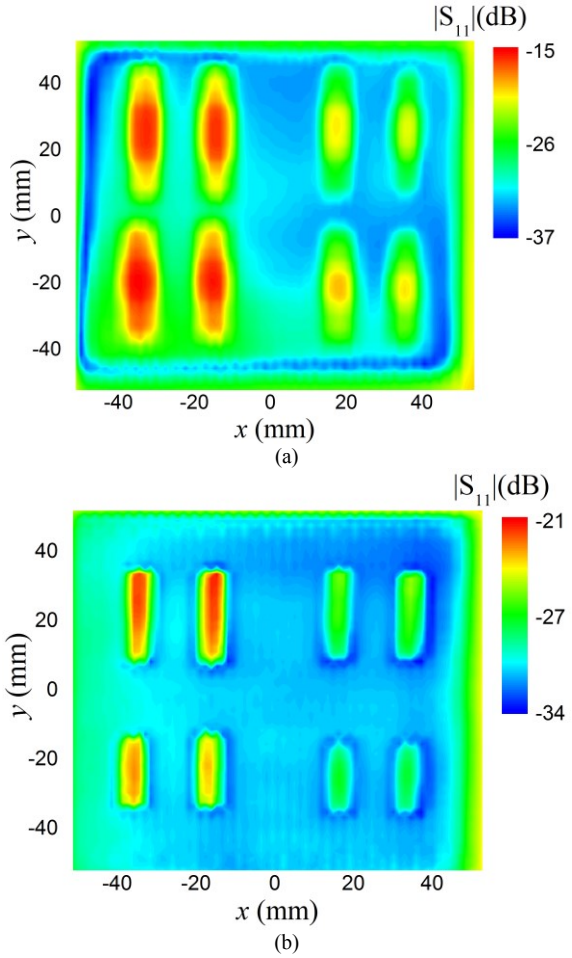

Fig.13. Amplitude reflection image of the dielectric imaging test composed of lossy BSR and GDS strips on the lossy FGM substrate obtained with (a)LA probe, imaging distance 5mm (b) helix antenna probe, imaging distance 2mm. Measurement step Δx=Δy=2mm.

It can be seen in Fig. 13 that the strips composed of BSR dielectric can be discriminated from the GDS dielectric strips with ~5dB and with more than 10dB from the FGM substrate with both LA and helix probes. Phase images (not presented for brevity) show resolution contrast of around 10° between the BSR and GDS strips and around 50° contrast from the FGM substrate. It should be noted that for the considered geometry of the sample, Fig.12, due to a different coupling mechanism of two probes, the imaging contrast for the helix antenna probe deteriorates significantly faster (amplitude contrast ~2dB at 5mm stand-off distance) than the contrast achieved with the LA probe. Simulations show that the electric field amplitude in the space between the probe and the FGM dielectric layer attenuates as z^{-2} for the helix antenna and as $z^{-1.5}$ for the LA probe. The last effect can be explained as a formation of a semi-open resonator between the LA plate, Fig.2, and dielectric surface which leads to slower field attenuation.

V. Imaging of Printed Circuit Board Samples

Reflection imaging of planar conductive elements printed on a dielectric substrate is important in printed circuit boards (PCB) assessment, non-destructive testing and defect finding in printed antenna arrays, etc.

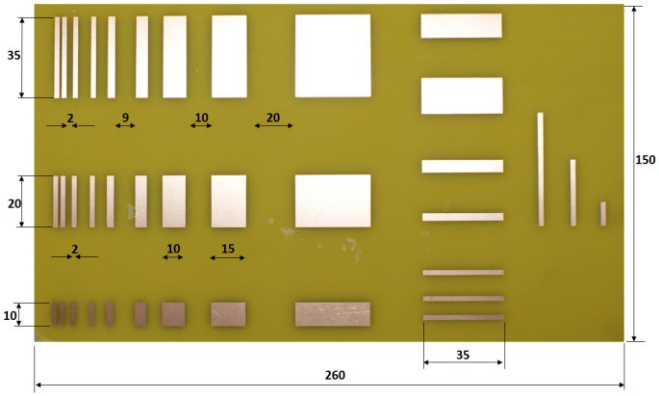

Fig.14. PCB imaging test structure, conductive strips on the 1.6mm thick FR4 substrate ($\varepsilon_r \approx 4$), all dimensions in millimeters. No ground plane is present at the back of the structure.

The first test sample, Fig.14, was designed in analogy with the dielectric imaging chart in Fig. 8, in order to allow spatial resolution and imaging contrast estimation for the considered resonance probes.

The reflection images obtained with the LA and helix (with the axis along the y range) probes are shown in Figs.15 and 16 respectively. The stand-off imaging distance is chosen to obtain approximately the same amplitude image contrast. The results of the measurements can be summarized as follows. The characteristic resolution in the case of the LA probe across the x range is 5mm at the 4mm standoff distance for both resonant (middle row of strips) and non-resonant, large (top row) conductive elements. It should be noted that the wavelength in dielectric corresponding to resonance frequency 4GHz is $\lambda_0/\varepsilon_r^{1/2}$ = 37.5mm, λ_0 is a wavelength in free space. Small elements of size $\lambda_0/7.5$ in the bottom row can also be clearly resolved for the x-range spacings more than 5mm. The amplitude imaging contrast is more than 10dB for all vertical strips. It can also be seen that the vertical resolution is approximately limited by the length of the insert, L_1, and

additional dual peak features arise as a consequence of dipole-like near field of the LA probe.

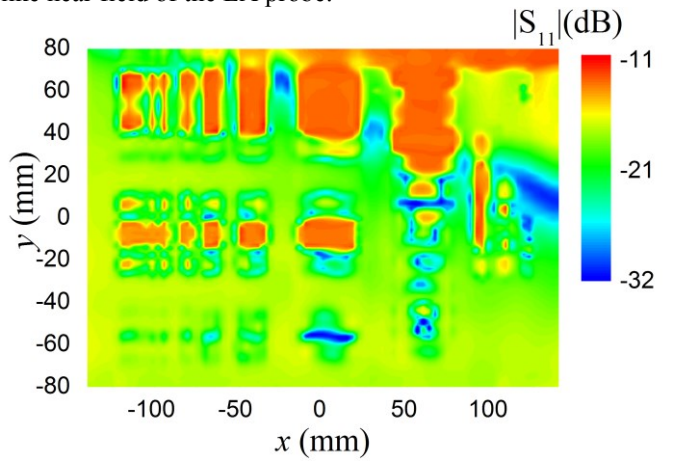

(a)

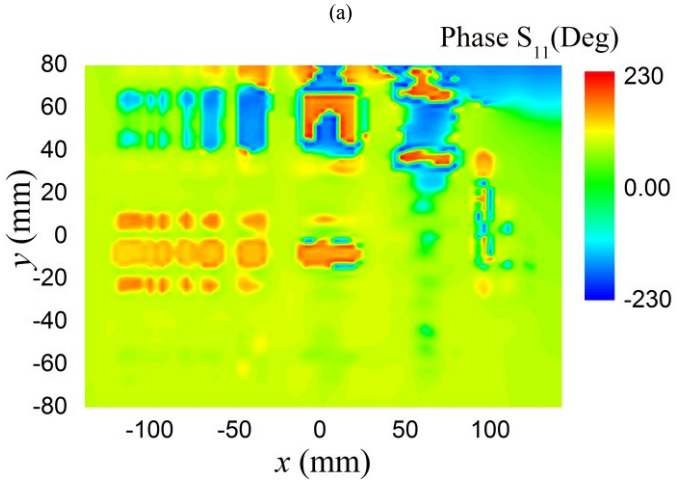

(b)

Fig.15. Raw reflection image amplitude (a) and phase (b) obtained with LA probe at 3.99GHz at the imaging distance 4mm. Measurement step Δx=Δy=2mm.

The phase image, Fig.15(b), displays high contrast (more than 100°) for top and middle row of vertical strips, however the bottom row cannot be clearly resolved. A series of measurements was carried out for different stand-off distances in the range 3-7mm. It was observed that the resonance frequency is reduced in analogy with a dielectric sample case, Fig.11, therefore scanning in narrow frequency band around the resonance is generally required.

Spatial imaging resolution and contrast reduce with larger stand-off distance, with spatial resolution approximately equal to the stand-off distance. The amplitude imaging contrast remains higher than 5dB in the 3-7mm imaging distance range.

The measurements carried out with the helix antenna, Fig.16, show equally high imaging contrast, both amplitude (~10dB) and phase (~40°) and high spatial resolution in both *x* and *y* range (5mm), however resolution significantly deteriorates with larger stand-off distance, more than two times at imaging distance *z* = 4mm.

The imaging test in Fig.14 can be extended to contain the conductive elements of complex geometric shape, Fig. 17(a).

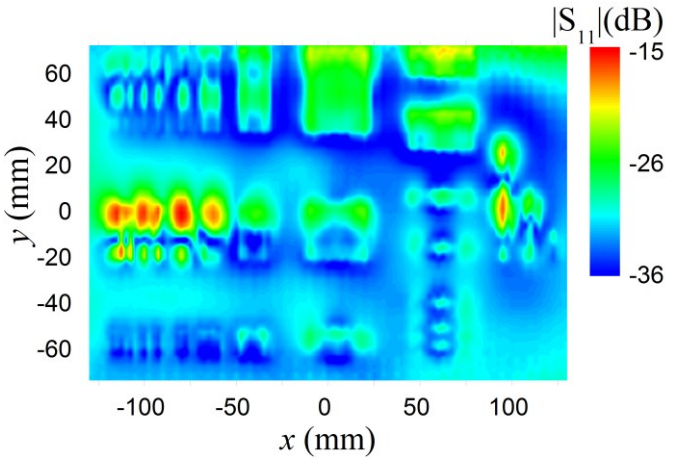

(a)

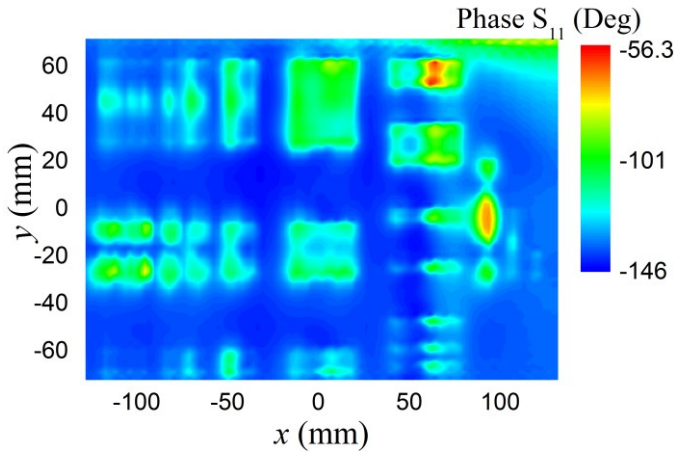

(b)

Fig.16. Raw reflection image amplitude (a) and phase (b) obtained with a helix probe with vertical axis orientation at 4.05GHz at the imaging distance 2mm, measurement step Δx=Δy=2mm.

The raw amplitude images obtained with the LA probe, Fig.17 (b) and helix antenna, Fig. 17(c) show that very high-contrast resolution (>15dB) can be achieved with both probes. The LA probe image possesses better quality for the top and middle row, as compared with the amplitude image obtained with the helix antenna.

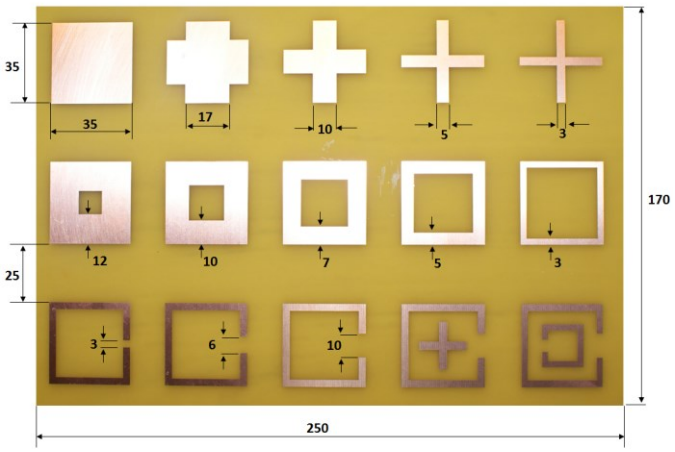

(a)

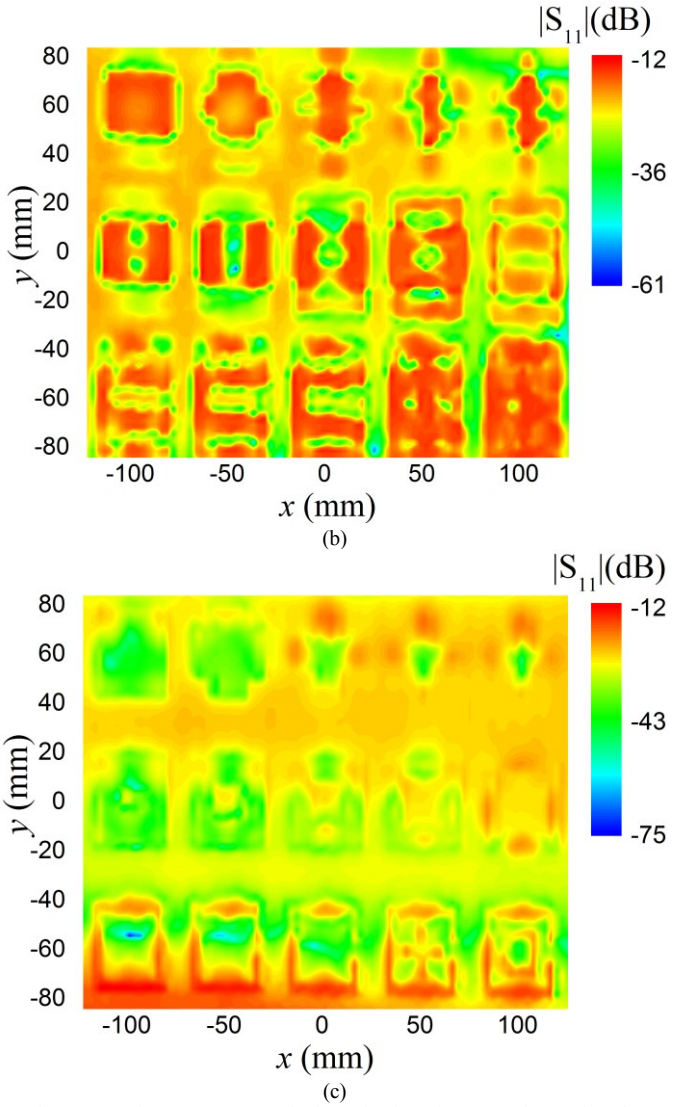

Fig.17. Imaging test composed of conductive elements of complex shapes printed on 1.6mm thick FR4 substrate, no ground on the back side (a). Raw amplitude images obtained with LA probe at 4.017GHz, (b) and vertical helix probe at 4.02GHz, (c). Imaging distance is 2mm, measurement step Δx=Δy=2mm.

It should be noted that the LA probe introduces distortion of the raw image due to its dual-peak near field pattern. This is clearly seen in Figs. 15 and 17(a). This distortion can be eliminated in some imaging scenarios using cross-correlation technique, as demonstrated in the next Section.

VI. Cross-Correlation Technique for Geometry Perturbation Characterization

Let us consider an imaging scenario, when there are two test samples, a "master" or "standard" test, Fig.18 (a) and a sample with defect element, Fig.18 (b) which is geometrically different from the corresponding "master" test element. This geometric difference can be very small in terms of the wavelength, with characteristic size less than λ/10. The purpose of this Section is twofold. Firstly we demonstrate how cross-correlation technique [42], [43] can be used to characterize small element deviations in the considered imaging scenario and secondly it will be shown that the dual-peak features present in the raw images obtained by the LA probe can be eliminated. Therefore in this Section we only use the measured data obtained with the LA probe.

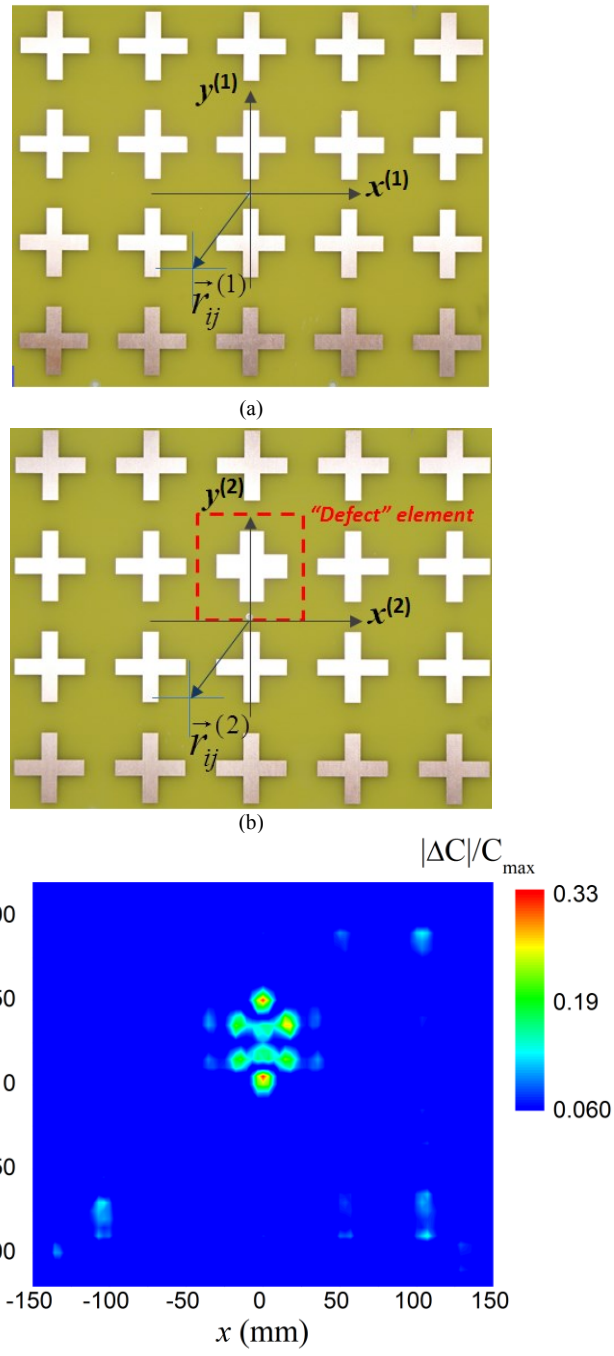

Fig.18.(a) "Master" imaging test (b) imaging test with "defect" element and (c) cross-correlation between "master" and "defect" test samples. The measured data obtained with the LA probe at 4.01GHz, 5mm stand-off distance. The "master" printed element consists of two crossed rectangles of 35mm length and 8mm width. The "defect" element consists of two crossed rectangles of 35mm length and 14mm width. Lattice dimensions 52mmx52mm. Imaging step Δx= Δy=2mm.

In the framework of the cross-correlation approach two measured S_{11}data sets are compared: the first set of S_{11} measured data belongs to the "master" test while the second set of S_{11} data belongs to the test with geometry deviations

("defect"). The measured data are compared for each measurement point with the same indices (i, j) , i=1,2,…N_x, j=1,2,…, N_y. N_x and N_y are the number of the measurement points along the x and y range correspondingly.

The computational procedure operates as follows. First, an auto-correlation function for the "standard" test is calculated for each measurement point $\vec{r}_{ij}^{(1)} = \left(x_i^{(1)}, y_j^{(1)}\right)$,

$$C_1\left(\vec{r}_{ij}^{(1)}\right) = R_1 \cdot R_1^* . \qquad (2)$$

In (2) R_1 is a complex-valued reflection coefficient for the (i, j) measurement point within the "standard" test measurement range, the asterisk symbol denotes complex conjugate. Next the cross-correlation between the measured S_{11} data for "standard" and "defect" samples is computed for the measurement points (i, j) as

$$C\left(\vec{r}_{ij}^{(1)}, \vec{r}_{ij}^{(2)}\right) = R_1 \cdot R_2^* \ , \qquad (3)$$

where R_2 is a complex-valued reflection coefficient for measurement point (i, j) for the "defect" element. The "defect" geometry deviation can be characterized by the normalized difference $f_d\left(\vec{r}_{ij}^{(1)}, \vec{r}_{ij}^{(2)}\right)$ of auto- and cross-correlation functions as

$$f_d\left(\vec{r}_{ij}^{(1)}, \vec{r}_{ij}^{(2)}\right) = \left|C_1\left(\vec{r}_{ij}^{(1)}\right) - C\left(\vec{r}_{ij}^{(1)}, \vec{r}_{ij}^{(2)}\right)\right| / C_{\max} \qquad (4)$$

where $C_{max} = \max[C_1, C_2]$ is a peak value of the autocorrelation function (2) or a counterpart autocorrelation function for the "defect" element $C_2\left(\vec{r}_{ij}^{(2)}\right) = R_2 \cdot R_2^*$.

The calculated normalized correlation function (4) is shown in Fig. 18(c) for the test samples in Fig 18(a) and(c). The "defect" element geometry deviation is ~3mm which is ~λ/25 at 4GHz. It can be seen that not only the defect position in the printed array is accurately detected but also the geometry perturbation ("defect") is clearly resolved with more than 15dB contrast from the average background level of the cross-correlation function (4) outside of the "defect" cell. It is important to note that the dual-peak feature of the LA probe, present in the raw images, e.g. Figs. 15, 17(a) is completely eliminated by the cross-correlation processing.

The demonstration of the cross-correlation technique can be extended further using the data for the test sample in Fig.17(a).

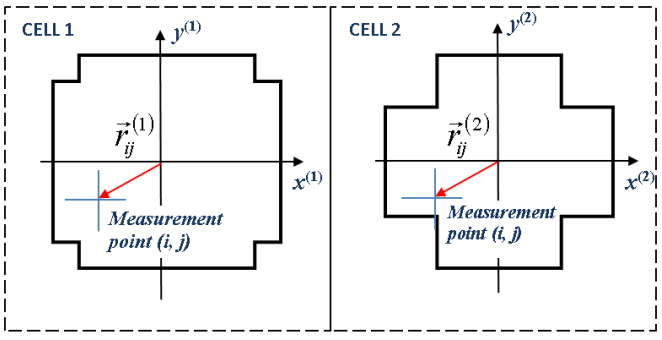

Fig.19. The S_{11} data are cross-correlated in the measurement points (i, j) within the "standard" (1) and "defect" (2) unit cells.

In this structure the printed elements are designed in such a way that their geometry gradually varies from element to element in each row. Calculating the cross-correlation (4) between the measured data in each unit cell, Fig.19, it is possible to reveal how small geometry deviation can be accurately characterized by the cross-correlation image processing.

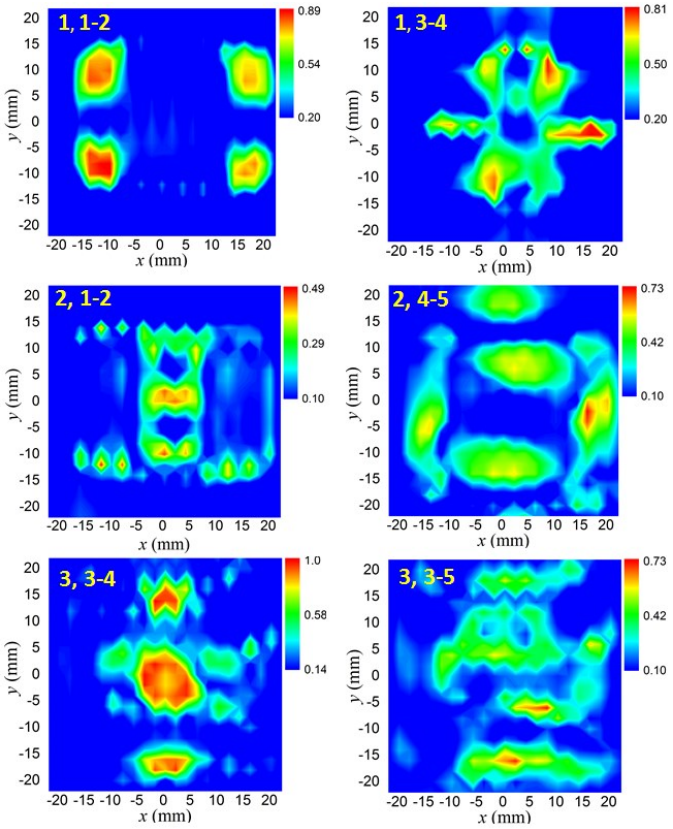

Fig.20. Normalized cross-correlation function (4) for the printed elements of the test sample shown in Fig.17(a).

To represent the results, we number the elements in the printed array structure in Fig.17 (a) as follows. The rows 1-3 are numbered from the left top corner of the sample, columns 1-5 are numbered from left to right, the unit cell size is chosen to be 42mmx42mm, measurement step Δx=Δy=2mm.

Fig. 20 shows the calculated cross-correlation function for the sample in Fig.17(a) using the LA probe S_{11} measured data. In this figure the elements positions are shown by a number string inserted in the top left corner of the graphs, e.g. 1,1-2 stands for the cross-correlation between the elements in the first row, first and second columns. The data in Fig.20 show that even small geometry difference between the elements can be precisely located in space and resolved with a very high contrast (more than 10dB). It is interesting to note that the elements features smaller than the vertical spatial resolution limit of the LA probe can be discriminated, e.g. elements in the cells (3,4) and (3,5). The cross-correlation of these elements with a split square loop element in the (3,3) cell show that the inner cross in the (3,4) cell element can be

clearly discriminated from the inner square loop in the (3,5) element, with data presented in Fig.20, bottom row. It is also important to note that dual-peak feature is eliminated by the image processing.

VII. Conclusions

A microwave high-resolution near-field imaging technique is proposed and experimentally evaluated in reflectometry imaging scenarios involving planar metal-dielectric structures. We consider two types of the resonance near field probes - a loaded subwavelength slot aperture and a small helix antenna. It is shown that these probes enable very tight spatial field localization in the near field zone with the full width at half maximum around one tenth of a wavelength, λ, at λ/20–λ/10 stand-off distance. Experimental results demonstrate that the proposed probes permit resonance electromagnetic coupling to the dielectric or printed conductive elements or patterns which leads to the possibility of a very high raw image resolution with contrast more than 10dB amplitude and 50 degrees phase. This near field dynamic range on magnitude and phase has not been previously achievable, to the best of authors' knowledge. Several imaging scenarios are considered, particularly it is shown that subwavelength dielectric structures of the same shape and size located on lossy dielectric substrate can be accurately discriminated based on their permittivity contrast which is highly sought in non-destructive testing and biomedical applications. Finally, a correlation-based technique was proposed for small geometry defect characterization in printed antenna arrays. Experimental results demonstrate that subwavelength geometry and symmetry defects with characteristic size ~ λ/15 and smaller can be detected and qualitatively characterized.

Acknowledgement

The Authors thank the anonymous Reviewers for insightful comments and suggestions.

References

[1] S. Kharkovsky and R. Zoughi, "Microwave and millimeter wave nondestructive testing and evaluation", *IEEE Instrum. Measurement Magazine,* pp. 26-37, Apr. 2007.

[2] M. Tabib-Azar, Tao Zhang, and S. R. LeClair," Oscillating Evanescent Microwave Probes for Nondestructive Evaluations of Materials", *IEEE Trans. Instrum. Measurements*, vol. 51, no. 5, pp. 1126 – 1132, Oct. 2002.

[3] S. Kharkovsky, A. Ryley, V. Stephen, and R. Zoughi, "Dual-polarized near-field microwave reflectometer for noninvasive inspection of carbon fiber reinforced polymer-strengthened structures," *IEEE Trans. Instrum. Meas*., vol. 57, no. 1, pp. 168–175, Jan. 2008.

[4] P. Mehta et al., "Microwave reflectometry as a novel diagnostic tool for detection of skin cancers", *IEEE Trans. Instrumentation Measurements*, vol. 55, no 4, pp. 1309-1316, Aug. 2006.

[5] M. Farina, A. Di Donato, D. Mencarelli, et al., "High Resolution Scanning Microwave Microscopy for Applications in Liquid Environment", *IEEE Microwave Wireless Components Lett*. vol. 22, no.11, pp.595-597, Nov. 2012.

[6] C. Colla, et.al., "Diagnostic by imaging: 3D GPR investigation of brick masonry and post-tensioned concrete", *13th Intl. Conf. Ground Penetrating Radar,* pp.1-7, 2010.

[7] R. Zoughi, *Microwave Non-Destructive Testing and Evaluation*. Kluwer, 2000.

[8] K. Haddadi, T. Lasri, "Geometrical Optics-Based Model for Dielectric Constant and Loss Tangent Free-Space Measurement", *IEEE Trans. Instrum. Meas*., vol. 63, no.7, pp. 1818-1823, July 2014.

[9] K. Haddadi, M. M. Wang, D. Glay, and T. Lasri,"Performance of a Compact Dual Six-Port Millimeter-Wave Network Analyzer", *IEEE Trans. Instrum. Meas.*, vol.60, no.9, pp. 3207-3213, Sept 2011.

[10] L. Handjojo, K.J. Bois, J. Bauer, R. Hamilton, and R. Zoughi, "Broad-band microwave dielectric property characterization of various glass specimens," *Nondestruct. Testing Eval*., vol. 16, pp. 55–69, 2000.

[11] Smart sensors for real-time water quality monitoring, S.C. Mukhopadhyay and A. Mason, ed., Springer, 2013.

[12] M. Ghasr, B.J. Carroll, S. Kharkovsky, R. Zoughi, and R. Austin, "Millimeter wave differential probe for nondestructive detection of corrosion precursor pitting," *IEEE Trans. Instrum. Meas*.,vol. 55, no. 5, pp.1620–1627, Oct. 2006.

[13] A. Taeb, S. Gigoyan, S. Safavi-Naeini, "Millimetre-wave waveguide reflectometers for early detection of skin cancer", *IET Microw. Antennas Propag.*, vol. 7, no. 14, pp. 1182–1186, 2013

[14] E.A. Ash and G. Nichols, Super-resolution aperture scanning microscope, *Nature* 237, 1972, pp. 510–512.

[15] O. Mitrofanov, et al, "Terahertz near-field microscopy based on a collection mode detector", Appl. Phys. Lett. vol. 77, pp. 3496-3499, 2000.

[16] T. Nozokido, N.Miyasaka, and J. Bae, "Near field slit probe incorporating a micromachined silicon chip for millimeter-wave microscopy", *Microwave and Optical technology Lett*., vol. 53, no. 3, pp. 660-664, Jan 2011.

[17] K.Haddadi and T. Lasri, "60-GHz Near-Field Six-Port Microscope Using a Scanning Slit Probe for Subsurface Sensing", *IEEE Sensors Journal*, vol.12, no. 8, pp. 2575 – 2577, Aug. 2012.

[18] G. C. Cho, H.-T. Chen, and S. Kraatz et al., "Apertureless terahertz near-field microscopy," *Semicond. Sci. Technol*., vol. 20, pp. S286–S292, 2005.

[19] K. Haddadi and T. Lasri, "Scanning microwave near-field microscope based on the multiport technology", *IEEE Trans. Instrum. Measurement*, vol. 62, no. 12, pp. 3189 – 3193, Dec. 2013.

[20] B. T. Rosner and D.l W. van der Weide, "High-frequency near-field microscopy", *Review of Scientific Instruments,* vol. 73, pp. 2505-2525, 2002.

[21] N. Klein, P. Lahl, U. Poppe, et.al.,"A metal-dielectric antenna for terahertz near-field imaging, *Journ. Appl. Physics*, 98, pp. 014910(5), 2005.

[22] S. Dieter, and W. Menzel,"High-Resolution probes for near-field measurements of reflectarray antennas", *IEEE Antennas Wireless Propagat. Lett*., vol.8, pp.157-160, 2009.

[23] J. Nadakuditi, G. Chen, R. Zoughi, "Semiempirical electromagnetic modelling of crack detection and sizing in cement-based materials using near-field microwave methods" *IEEE Trans. Instrum. Measurements*, vol. 55, no.2, pp. 588-597, Apr. 2006.

[24] R. K. Amineh, M. Ravan, A. Trehan, and Natalia K. Nikolova, "Near-Field microwave imaging based on aperture raster scanning with TEM horn antennas*", IEEE Trans. Antennas Propagat.,* vol. 59, no.3, pp. 928-940, March 2011.

[25] S. Kharkovsky, A. McClanahan, R. Zoughi, D. Palmer, "Microwave dielectric-loaded rectangular waveguide resonator for depth evaluation of shallow flaws in metals" *IEEE Trans. Instrum. Measurements*, vol. 60, no.12, pp. 3923-3930, Dec. 2011.

[26] H. A. Bethe, "Theory of diffraction by small holes," Phys. Rev., vol. 66, pp. 163–182, 1944.

[27] Y. Kawano, "Highly sensitive detector for on-chip near-field THz imaging," *IEEE J. Sel. Topics Quant. Electron*., vol. 17, no. 1, pp. 67–78, 2011.

[28] T. Pochiraju, O. Malyuskin, and V. Fusco, "Tunable near-field subwavelength microwave imaging," *Microw. Opt. Technol. Lett*., vol. 53, no. 6, pp. 1229–1231, 2011.

[29] O. Malyuskin, V. Fusco, "Near field enhancement and subwavelength imaging using resonantly loaded apertures", *IEEE Trans Antennas Propagat,* vol. 62, no. 6. 2014, pp. 3130-3140.

[30] M. Kanda, "Standard probes for electromagnetic field measurements", *IEEE Trans. Antennas Propagat*., vol. 41, no.10, pp. 1349-1364, Oct 1993.

[31] G.Smith, "The electric-field probe near a material interface with application to the probing of fields in biological bodies", *IEEE Trans. Microwave Theory Techniques*, vol. 27 no.3, pp. 270-278, 1979.

[32] B. McLaughlin, P. Robertson, "Submillimeter coaxial probes for dielectric spectroscopy of liquids and biological materials", *IEEE Trans. Microwave Theory Techniques*, vol. 57, no.12, pp. 3000-3010, 2009.
[33] T. Pochiraju , O. Malyuskin, V. Fusco, "Sub-wavelength near field imaging using a non-resonant slot with a wire insert", *IEEE Antennas Propagat. Int. Symp*, pp.1-4. 2010.
[34] C. Balanis, *Antenna Theory*. Wiley, 1997.
[35] M. D. Weiss, B. Zadler, S.t Schafer, and J. Scales, "Near field millimeter wave microscopy with conical Teflon probes", *Journ. Appl. Physics*, vol. 106, 044912(8), 2009.
[36] O. Malyuskin and V. Fusco , "Resonantly loaded apertures for high-resolution near-field surface imaging", *IET Science, Measurement & Technology*, DOI: 10.1049/iet-smt.2014.0337, 14 April 2015.
[37] A. Ludwig, C. D. Sarris, and G. V. Eleftheriades, "Near-Field antenna arrays for steerable sub-wavelength magnetic-field beams", *IEEE Trans. Antennas Propagat*., vol. 62, no.7, pp.3543-3551, July 2014.
[38] L Markley, G. V. Eleftheriades, "A Near-field probe for subwavelength-focused imaging", *IEEE Trans. Microwave Theory Techniques*, vol. 58, no.3, pp. 551-558, March 2010.
[39] J. D. Kraus, "The helical antenna," *Proc. of the IRE*, vol. 37, no. 3, pp. 263-272, March 1949.
[40] Nearfield Systems Inc, www.nearfield.com
[41] http://www.eccosorb.eu/products/eccosorb
[42] M.A. Sutton, J.-J. Orteu, H. W. Schreier, *Image Correlation for Shape, Motion and Deformation Measurements*, Springer, 2009.
[43] S.F. Gregson, J. McCormick, C. Parini, *Principles of Planar Near-field Antenna Measurements*. IET, UK 2007.